Ion chamber and film-based quality assurance of mixed electron-photon radiation therapy

Veng Jean Heng*
Department of Physics & Medical Physics Unit, McGill University, Montreal

Monica Serban
Department of Medical Physics, McGill University Health Centre, Montreal

Jan Seuntjens
Medical Physics Unit, McGill University and Research Institute of the McGill University Health Centre, Montreal

Marc-André Renaud
Department of Mathematics & Industrial Engineering, Polytechnique Montréal, Montreal

(Dated: June 25, 2021)

Purpose: In previous work, we demonstrated that mixed electron-photon radiation therapy (MBRT) produces treatment plans with improved normal tissue sparing and similar target coverage, when compared to photon-only plans. The purpose of this work was to validate the MBRT delivery process on a Varian TrueBeam accelerator and laying the groundwork for a patient-specific quality assurance (QA) protocol based on ion chamber point measurements and 2D film measurements.

Methods: MC beam models used to calculate the MBRT dose distributions of each modality (photons/electrons) were validated with a single-angle beam MBRT treatment plan delivered on a slab of Solid Water phantom with a film positioned at a depth of 2 cm. The measured film absorbed dose was compared to the calculated dose.

To validate clinical deliveries, a polymethyl methacrylate (PMMA) cylinder was machined and holes were made to fit an ionisation chamber. A complex MBRT plan involving a photon arc and three electron delivery angles was created with the aim of reproducing a clinically realistic dose distribution in typical soft tissue sarcoma tumours of the extremities. The treatment plan was delivered on the PMMA cylinder. Point measurements were taken with an Exradin A1SL chamber at 2 nominal depths: 1.4 cm and 2.1 cm. The plan was also delivered on a second identical phantom with an insert at 2 cm depth, where a film was placed.

An existing EGSnrc user-code, SPRRZnrc, was modified to calculate stopping power ratios between any materials in the same voxelised geometry used for dose calculation purposes. This modified code, called SPRXYZnrc, was used to calculate a correction factor, k_{MBRT}, accounting for the differences in electron fluence spectrum at the measurement point compared to that at reference conditions. The uncertainty associated with neglecting potential ionisation chamber fluence perturbation correction factors using this approach was estimated.

Results: The film measurement from the Solid Water phantom treatment plan was in good agreement with the simulated dose distribution, with a gamma pass rate of 96.1% for a 3%/2 mm criteria. For the PMMA phantom delivery, for the same gamma criteria, the pass rate was 97.3%. The ion chamber measurements of the total delivered dose agreed with the MC-simulated dose within 2.1%. The beam quality correction factors amounted to, at most, a 4% correction on the ion chamber measurement. However, individual contribution of low electron energies proved difficult to precisely measure due to their steep dose gradients, with disagreements of up to 28% $\pm$ 15% at 2.1 cm depth (6 MeV). Ion chamber measurement procedure of electron beams was achieved in less than 5 minutes, and the entire validation process including phantom setup was performed in less than 30 minutes.

Conclusion: The agreement between measured and simulated MBRT doses indicates that the dose distributions obtained from the MBRT treatment planning algorithm are realistically achievable. The SPRXYZnrc MC code allowed for convenient calculations of k_{MBRT} simultaneously with the dose distributions, laying the groundwork for patient-specific QA protocol practical for clinical use. Further investigation is needed to establish the accuracy of our ionisation chamber correction factors k_{MBRT} calculations at low electron energies.

Running title: Ion chamber and film-based QA of MBRT

* Corresponding author: veng.heng@mail.mcgill.ca
1001 Boulevard Décarie Rm. DS1.502
Montréal, QC, H4A 3J1, Canada

I. INTRODUCTION

The majority of patients undergoing external beam radiation therapy (EBRT) are treated with photons beams, while electron beams, despite being available in the medical linear accelerators, are only used in the treatment of a limited number of disease sites. All available photon and electron energies constitute modalities that could potentially be combined into a mixed beam (MBRT) plan to produce a superior treatment plan compared to single-energy, single-particle plans, provided that MBRT delivery is logistically feasible within the clinical workflow.

The modulated electron radiation therapy (MERT) literature has historically focused between studying MERT delivery using tertiary electron-specific collimators such as the eMLC [1–5] or the few-leaf electron collimator (FLEC) [6–8], and the approach of utilising the photon MLC (pMLC) already present in modern linacs [1, 9–12]. Early studies showed that a shortened source-to-surface distance (SSD), typically 70 cm, was necessary to produce clinically acceptable electron dose distributions due to the degradation of electron field penumbras in air [13]. Traditional electron RT remains cumbersome to deliver in comparison to photon RT, requiring custom patient-specific cut-outs and more time consuming setup. Despite the fact that MERT delivered using tertiary collimators has been shown to be accurate [8], MERT has seen limited adoption in the clinic due to time consuming tasks related to set-up and commissioning compared to conventional photon RT, and also due to the high plan quality of modern intensity modulated (IMRT) and volumetric modulated arc therapy (VMAT) dose distributions.

However, there remains an important subset of patients with tumours with a superficial component that would benefit substantially from the limited range of electron radiation to spare organs at risk (OAR) downstream from the tumour. In recent years, there has been a renewed interest in pMLC-based MERT delivery in the context of mixed electron-photon beam treatments. Previous planning studies have shown that, while electron-only MERT treatment plans typically deliver lower doses to normal tissue compared to photon plans, they are unable to provide the same level of dose homogeneity within the target [12, 14]. On the other hand, pMLC-based MBRT plans have recently been shown to provide superior OAR sparing compared to IMRT or VMAT plans without sacrificing target coverage [15–18].

MBRT plans delivered using a pMLC as the sole collimation device would be the simplest to integrate into the clinical workflow as they do not, in principle, require staff intervention when switching modalities. Miguez et al. have demonstrated that pMLC-based MBRT for accelerated partial breast irradiation (APBI) can be implemented safely in the clinic. They also performed pre-treatment QA through ion chamber and film measurements on a hemispherical phantom. However, the treatment deliveries typically involved only three gantry angles and fewer than 10 fields. Furthermore, the method used to convert ion chamber readings to dose to water or dose to medium was not described [19]. Recently, Mueller et al. have delivered one brain and two head & neck MBRT plans with a non-coplanar photon component onto an anthropomorphic Alderson head phantom with films and shown 2%/2 mm gamma pass rates above 99.2% for all cases when compared to the expected simulated dose distribution [18], supporting the notion that MBRT using the pMLC can be delivered accurately. However, while the photon delivery was more complex than in the work of Miguez et al., the electron component remained simple, with one or two apertures per energy per beam angle. In addition, the delivered treatment plans did not contain low energy (6 or 9 MeV) components, which are likely to be the most challenging to model accurately. Due to their steep dose gradients, these low energies are also the most problematic for point measurements.

In this work, we present comparisons between simulated and measured MBRT dose distributions for a simple, inherently robust delivery and a complex delivery. The aim was to 1) validate that the MC beam model used to produce MBRT treatment plans could accurately determine the number of MUs necessary to produce a desired dose distribution from each modality, 2) present a methodology for calculating beam quality correction factors for ionisation chamber measurements in MERT and MBRT fields and 3) validate the accuracy of clinical MBRT deliveries using point measurements with an ionisation chamber and film dosimetry.

II. METHODS

A. Reference dose measurements for MLC-defined electron fields

Reference dose calibration for the applicator-less electron beams was performed on a Varian TrueBeam linear accelerator using an IBA Blue Phantom 2 water tank and an Exradin A1SL ionisation chamber. The reference conditions were defined to be 80 cm source-to-surface distance (SSD), with the MLC leaves positioned to define a 10 x 10 cm^2 field when projected at the machine isocenter. This choice of non-standard reference conditions was made to closely align the reference conditions with the delivery conditions for the electron component of MBRT plans. Although shorter SSDs lead to better electron penumbras, typical MBRT plans have SSDs closer to 80 cm in order to provide safer gantry clearance. The jaws were set to 35 x 35 cm^2, which is slightly larger than the largest allowable

MLC field for our MBRT planning algorithm. MLC leaves were restricted to a 30 cm field in their direction of motion due to their maximum leaf span of 15 cm. Reference dose measurements were performed at d_{ref} following the AAPM Task Group 51 (TG-51) protocol [20].

The charge measured in the ionisation chamber was converted to absorbed dose to water using equation 1,

$$D_{ref}(d_{ref}) = M_c \; k_{Q,ecal} \; k_Q^{'} \; N_{D,w}^{Co} \tag{1}$$

where M_c is the ionisation chamber reading, corrected for environmental conditions, ion recombination and polarity, $k_{Q,ecal}$ and $k_Q^{'}$ are the beam quality conversion factors described in Muir et al., (2014) [21]. The A1SL $N_{D,w}^{Co}$ coefficient used in this work was traceable to national primary absorbed dose standards.

The conversion factors are similar to $k_{R_{50}}$ and k_{ecal} described in the TG-51 report [20] but explicitly take into account P_{gr}, the gradient correction for the ionisation chamber used in this work. The values for the beam quality conversion factors were obtained from the Monte Carlo work by Muir et al., (2014) [21]. While these conversion factors were calculated in standard reference conditions at 100 cm SSD rather than the reference conditions used in this work, they are specified in terms of R_{50} which we assume remains a faithful specification of the beam quality and, hence, electron fluence spectrum at the reference point for an 80 cm SSD setup.

B. Absorbed dose measurements in MBRT fields

Ionisation chambers are calibrated in terms of dose to water at the reference depth for a specific beam quality. The k'_Q beam quality correction factors used in eq. 1 are therefore only valid for the reference conditions described in section II A. When attempting to perform measurements in MBRT fields, we must correct the ionisation chamber response for the exact electron fluence spectrum at the point of measurement in the MBRT field, which can vary greatly from the electron fluence spectrum in reference conditions.

Differences in electron fluence spectrum can be caused by differences in measurement depth as well as by intensity modulation and delivery from multiple angles. The electron apertures for a given energy may not deliver radiation directly aimed at the measurement point, as shown in figure 1, leading to a potentially different electron fluence spectrum compared to reference conditions.

The beam quality conversion factor is defined as the ratio of the ratio of absorbed dose to water, D_w, to the absorbed dose in the air cavity of the ionisation chamber, D_{ch}, between a beam quality Q and cobalt-60,

$$k_Q = \left(\frac{D_w}{D_{ch}}\right)_{Co}^{Q}. \tag{2}$$

This ratio can be calculated with Monte Carlo methods assuming a fully characterised model of the ionisation chamber is included in the calculation [21–23]. In the methodology underlying AAPM's TG-51 protocol, however, this ratio was approximated as a ratio of Spencer-Attix stopping power ratios corrected for fluence perturbations,

$$k_Q \approx \frac{\left[\left(\frac{\bar{L}}{\rho}\right)_{air}^{water} P_{cel}P_{fl}P_{wall}P_{gr}\right]^{Q}}{\left[\left(\frac{\bar{L}}{\rho}\right)_{air}^{water} P_{cel}P_{fl}P_{wall}P_{gr}\right]^{Co}}, \tag{3}$$

where $\left(\frac{\bar{L}}{\rho}\right)_{air}^{w}$ is the Spencer-Attix stopping power ratio (SPR) between water and air [24]. In this work we followed the latter methodology to apply a conversion factor between the beam quality in reference condition and the MBRT fields,

$$k_{MBRT} = \left(\frac{D_w}{D_{ch}}\right)_{Q}^{MBRT}. \tag{4}$$

While an evaluation of eq. 4 requires a MC simulation of the local electron fluence with inclusion of the full chamber geometry, we assume that the first order contribution to k_{MBRT} is due to stopping power-ratio differences between

water and air for the MBRT beam quality and the reference beam quality and sufficiently accurately corrects for the difference in chamber response between these two situations. This approximation ignores electron fluence *perturbation* by the presence of the ionisation chamber, but does capture the differences in energy response of the detector between reference conditions and MBRT conditions. A similar approach was used in the work by Al-Yahya et al. to successfully calibrate nonstandard electron fields created by the FLEC. [6]

$$k_{MBRT} \approx \frac{\left[\left(\frac{\bar{L}}{\rho}\right)^{w}_{air}\right]^{MBRT}}{\left[\left(\frac{\bar{L}}{\rho}\right)^{w}_{air}\right]^{Q}}. \tag{5}$$

With this correction factor, the dose measured by an ionisation chamber in MBRT fields at depth d is given by:

$$D(d) = M_c \; k_{Q,ecal} \; k_Q^{'} \; k_{MBRT} \; N_{D,w}^{Co}. \tag{6}$$

To obtain the SPRs for each electron component, we imported the stopping power ratio scoring routines and reporting routines from the SPRRZnrc EGSnrc user-code [25] into the DOSXYZnrc code, so that stopping power ratio distributions can be scored in parallel with patient dose distributions in the same voxelised geometry as DOSXYZnrc. This modified code, SPRXYZnrc, thus allows a SPR distribution to be obtained in the same geometry with the same input file as the one used for DOSXYZnrc. For each electron beam energy, the SPR values between water and air for voxels inside the chamber volume of the phantom were averaged based on the weight of each field and used to determine k_{MBRT}. Within this paper, any mention of "field" refers to the radiation region resulting from a single MLC aperture.

C. Phantom simulation and planning

A cylindrical polymethyl methacrylate (PMMA) phantom, shown in figure 2, was machined for the purpose of this work. The aim was to produce a phantom with a geometry similar to a patient extremity to perform QA measurements on MBRT plans created for soft tissue sarcomas of the leg. Typical superficial extremity soft tissue sarcoma cases suitable for the MBRT technique have targets depths $\leq$ 6 cm. For ionisation chamber measurements, two holes were drilled with centres at depths of 1.4 cm and 2.1 cm from the surface of the cylinder, respectively. These two lateral depths were chosen as they represent the depth d_{max} of maximum dose at 6 and 9 MeV respectively. Due to the steep dose falloff at these energies, these relatively shallow depths are required to measure a substantial dose. The longitudinal depth of the holes was chosen such that the active volume of an ionisation chamber would align with the centre of the phantom, along its axis. A second identical PMMA phantom was machined and sliced along its length to create an insert for the placement of a Gafchromic EBT3 film (see Fig. 3). The horizontal slice is positioned at a depth of 2 cm from its top lateral face.

A Solid Water (Sun Nuclear Corporation, Melbourne, Florida) slab phantom, used for standard clinical QA was also involved in these experiments. CT simulation scans of the PMMA cylinders and the Solid Water slabs were obtained. During scanning of the PMMA phantom for the ionisation chamber measurements, an Exradin A1SL (Standard Imaging, Madison, Wisconsin) chamber was present in the 1.4 cm insert in order to contour the active volume of the chamber for SPR calculation purposes. CT markers were placed using the in-room lasers for reproducible positioning. The MBRT treatment planning algorithm described in Renaud et al. [16] was used to create treatment plans for the Solid Water slab and the PMMA cylinder. For the PMMA phantoms, the plan was optimised on the chamber phantom and then identically replicated on the film phantom for calculation and delivery purposes.

For the Solid Water slab phantom, a simple MBRT plan was created with a single electron beam angle (0°) while the photon component was composed of an arc from -110° to 110°. A total of 50 apertures spread across 6, 9, 12 MeV electrons and 6 MV photons were included in the treatment plan. The aim was to ensure that many modalities participated in the plan while maintaining a simple plan delivery rather than producing a clinically realistic plan.

The plan created for the PMMA cylinder aimed to reproduce a clinically realistic plan for a superficial target on the top half of the cylinder. The electron beam angles were (-30, 0, 30)° and the photon component was an arc from -110° to 110°. The electron component included a total of 40 electron apertures and was delivered as a step-and-shoot delivery. The beam delivery parameters for each plan are summarised in table I.

Figure 4 shows dose colourwashes for a representative axial slice for both plans. For both phantoms, the target is contoured in red. In both cases, the dose distribution is normalised so that 95% of the PTV volume receives 50 Gy.

D. Calculated dose distributions

In previous work, we have demonstrated PTV-based and CTV-based robust treatment planning algorithms to produce MBRT plans from beamlet-based apertures [16, 26]. However, beamlet-based apertures require a final MC recalculation to account for the effects of MLC leaves and jaw position on the dose distribution and the relative output of each aperture. In this work, each aperture of the treatment plans created for measurement purposes was recalculated using a validated MC beam model, and the MC dose distributions were renormalised from dose per primary particle to dose per monitor unit. At the time of MC recalculation, for photon arcs, MLC leaf movements at any gantry angle are interpolated between its two adjacent apertures.

MC simulations were performed using the phase space files distributed by Varian for the TrueBeam linear accelerator as the particle source (Virtual Linac) [27]. Particles sampled from the phase space files were transported through a BEAMnrc model consisting of the jaws, the base plate, the Millenium 120 MLC and the exit window [28]. Particles were further transported in a voxelised geometry by using DOSXYZnrc [29, 30]. The electron transport cutoff (ECUT) was 0.7 MeV, and the photon cutoff (PCUT) was 0.01 MeV. The EXACT boundary crossing algorithm was used, with a skin depth of 3 mean free paths. The electron stepping algorithm was PRESTA-II. The voxel sizes used in the MC simulations were 2 x 2 x 1 mm^3, where 1 mm was used along the depth axis. For SPR calculations, an ECUT of 0.521 MeV was used instead of 0.7 MeV.

The beam model and the phase space files were validated through measurements of output factors, depth doses and profiles of MLC-defined electron fields. The average energy of particles in some phase space files were tuned to better match measurement data. As such the average energy of electrons in the 6 MeV, 9 MeV and 12 MeV phase spaces were uniformly increased by 3%, 2% and 1% respectively.

To convert MC dose values into absorbed dose per Monitor Unit (Gy/MU), the MC reference dose calibration factors were obtained by reproducing the conditions described in section II A in a Monte Carlo simulation, and noting the MC dose per primary particle value at d_{ref} for each energy. The MC aperture dose distributions were then renormalised as

$$D_{MU}^{MC} = D^{MC} \frac{D_{ref}^{meas}}{D_{ref}^{MC}} \tag{7}$$

where D_{ref}^{meas} was the measured dose per MU in reference conditions, and D_{ref}^{MC} was the MC dose per primary particle calculated in the same reference conditions [31]. A monitor chamber backscatter correction was not applied as it has been shown that the correction is negligible when the jaw opening is kept sufficiently large and especially when MLC leaves are used to collimate the field [32]. The same procedure was performed to renormalise photon MC aperture dose distributions, however the reference conditions were taken as standard TG-51 conditions rather than the 80 cm SSD setup done for electrons.

The same treatment planning optimisation criteria were then used to re-optimise the relative weight of each aperture using the MC-calculated aperture dose distributions and obtain the monitor units for each aperture. The number of monitor units delivered from each modality for both plans is given in table II.

E. Phantom setup and delivery

The phantoms were positioned such that the distance between the geometric centre of the PTV and the source was 80 cm for the electron component (i.e. a virtual 80 cm SAD) and 100 cm for the photon component. The plans were delivered on a Varian TrueBeam linear accelerator, which has a nominal SAD of 100 cm, hence shortened SAD deliveries require a different couch position for each beam delivery angle.

The treatment plans were delivered using the TrueBeam developer mode which allows the couch to be moved dynamically during treatment. The setup and delivery process was as follows:

1. The phantom was positioned on the treatment couch and the CT markers were aligned with the in-room lasers.

2. The couch positions (lat, lng, vrt) displayed on the treatment console were recorded.

3. Using our in-house treatment planning system (TPS), the position of the machine isocenter in the CT coordinate system was identified, as shown in Fig. 5 (a), to establish a transformation between the couch coordinate system and the CT coordinate system.

4. The treatment plan was exported as an XML file using our TPS by supplying the information shown in Fig. 5 (b). The TPS automatically creates the XML files necessary for delivery using the TrueBeam developer mode and determines the couch position of each control point based on the transformation between the couch and CT coordinate systems shown in eq. 8.

5. The treatment plan was delivered on a per-modality basis, as the TrueBeam developer mode does not yet support changing between photon or electron energies within a single XML file.

The couch positions for each control point were determined using a simple translation of the couch based on the difference between the machine isocenter position at each control point and the machine isocenter in the setup position:

$$^{couch}_{cpt} = p^{couch}_{setup} + (p^{CT}_{cpt} - p^{CT}_{setup}). \tag{8}$$

F. Measurement setup

For the Solid Water phantom, a Gafchromic EBT3 film was placed at a depth of 2 cm and irradiated with all components of the treatment plan. The film was scanned 22 hours after irradiation using an Epson Expression 11000XL flatbed scanner (Epson America, Inc., Long Beach, CA). The film was then read into FilmQA Pro 2015 (Ashland Advanced Materials, Bridgewater, New Jersey) and the red colour channel was converted to dose using calibration films obtained on the same day. A single electron energy (12 MeV) was used to create the calibration curve. Gafchromic EBT3 films have been found to be suitable for measurements of mixed photon-electron dose distributions due to their low energy dependence in this energy range [33]. This film measurement procedure was repeated on the PMMA film phantom at a depth of 2 cm. In this case, in addition to an overall plan delivery, film measurements were also taken for each individual component of the treatment plan.

For the film measurement on Solid Water slabs, the total plan delivery was divided into 31 fractions and a single fraction was delivered on the film. The number of fractions was chosen such that the maximum dose on the film was approximately 70% of the maximum film calibration dose. This fractionation selection process was applied to each energy component individually delivered on the PMMA film phantom.

The ionisation chamber measurements were performed using an Exradin A1SL chamber inside a Solid Water plug inserted into the 1.4 cm hole of the PMMA cylinder. To ensure the reproducibility of the setup, the chamber measurement was repeated 3 times. For each measurement, the phantom was fully repositioned as described in section II E. The measurement process was repeated with the chamber and the Solid Water plug inserted in the 2.1 cm hole. The phantom was rotated such that the chamber was always positioned on the top half of the phantom. For the full delivery, a chamber measurement was also taken in the Solid Water slab phantom at 3.4 cm depth. The MBRT plan MC doses for all modalities were recalculated to account for the differences in materials between the planning and measurement conditions. The active volume of the ionisation chamber was converted from air to water in the MC simulation as the chamber is calibrated in terms of absorbed dose to water and thus nominally reports absorbed dose to water. Figure 6 shows the materials and densities used for the MC dose calculation. The same phantom was used to calculate SPRs inside the chamber volume.

G. Uncertainty estimation

In determining the uncertainty associated with the measured dose, D_{meas}, we combined the standard uncertainty on the reference dose determination (1.1%) with the uncertainties associated with the determination of k_{MBRT}, most notably by estimating the uncertainty associated with omitting the cavity fluence perturbation correction (p_{cav}) in the determination of k_{MBRT}, and a dose non-uniformity uncertainty based on the heterogeneity of the dose inside the chamber volume calculated using the MC doses.

The uncertainty associated with neglecting the fluence perturbation correction in the MBRT field was estimated by first assigning a hypothetical beam quality to each energy of the MBRT delivery ($R_{50,MBRT}$). This specifier was determined by inverting the $\left(\frac{\bar{L}}{\rho}\right)^{w}_{air}$ to R_{50} relationship given in the IAEA TRS-398 report, Appendix B, based on the $\left[\left(\frac{\bar{L}}{\rho}\right)^{w}_{air}\right]^{MBRT}$ values calculated using SPRXYZnrc. This hypothetical $R_{50,MBRT}$ was then used to obtain a value for $p_{cav,MBRT}$ using the equation for p_{cav} for cylindrical chambers as a function of R_{50} provided by TRS-398 Appendix B [34], which is based on a broad set of experimental data. $p_{cav,ref}$ was determined from the same formula but using the reference beam R_{50} instead. The relative difference between $p_{cav,MBRT}$ and $p_{cav,ref}$ (i.e., $1.0 - p_{cav,MBRT}/p_{cav,ref}$) does not exceed 1% and was treated as an uncertainty factor.

The uncertainty due to the non-uniformity of the dose inside the chamber volume was determined based on the minimum and maximum dose values inside the volume, and assuming a triangular distribution (i.e., $(D_{max} - D_{min})/D_{avg}/\sqrt{6}$).

III. RESULTS

A. Reference dose measurements

Table III shows the calibration depths and values measured in the applicator-less electron radiation therapy reference conditions described in section II A. The R_{50} beam quality specifiers were obtained from percent depth dose curves measured using an IBA RFD 3G diode detector (Ion Beam Applications, Louvain-la-neuve, Belgium) in the same reference conditions. For comparison, the R_{50} in table III are at most 5.6% larger (6 MeV) than if they were to be measured in standard reference conditions (100 cm SSD). The Type-A uncertainty on the MC-calculated SPRs was less than 0.2% for all modalities. All uncertainties stated are k = 1.

B. Film measurements

Fig. 7 & 8 present the results of the comparison between the film measurement and the planned dose distribution for the overall delivery on the Solid Water slabs and the PMMA cylinder respectively. Both a 3%/2mm and 2%/2mm global gamma analysis were performed with a global 10% dose threshold. The pass rates for either criterion are shown in table IV. The average type-A MC uncertainty on voxels with more than 50% of the maximum dose was less than 1%. It should be noted that MC uncertainty can artificially inflate the gamma pass rate. The gamma pass rates at 3%/2mm for the deliveries on both the cylindrical (97.3%) and Solid Water slab phantoms (96.1%) were found to be superior to the 95% pass rate tolerance limit recommended in TG218 [35] for IMRT QA. Only the 6 MeV component was found to have large discrepancies. However, at this low energy, it was found that the 2D dose distribution was highly sensitive to depth. Indeed, by varying the depth of the film slice by 1 mm in the MC calculation, the gamma pass rate at 2%/2mm increased from 62.1% to 99.5%.

C. Ionisation chamber measurements

To replicate clinical deliveries, the total dose from the PMMA treatment plan was divided into 20 fractions ($N_{frac} = 20$) and a single fraction was delivered in the measurement setup described in section II F. The plan MU shown in table II are therefore divided by ($N_{frac} = 20$) for a single measurement delivery.

Table V shows the measured dose values in the ionisation chamber compared to Monte Carlo-calculated doses for each modality. For each modality, $\left[\left(\frac{\bar{L}}{\rho}\right)^{w}_{air}\right]^{MBRT}$ was Monte Carlo-calculated using the SPRXYZnrc code with the same geometry and particle source as for the dose calculation performed in DOSXYZnrc. The MBRT beam quality correction factor, k_{MBRT}, was then determined using eq. 4 using the reference SPRs in table III. The absorbed dose to water was then calculated using eq. 6.

The largest difference between measurement and calculation were observed at 6 MeV with a discrepancy of 8.3% ± 7.5% and 28% ± 15% at 1.4 cm and 2.1 cm depth respectively. However, for the sum of all electrons at 1.4 cm depth, the measured dose and calculated dose agreed to within 0.5% and the total dose at the measurement point agreed to within -0.03%. At 2.1 cm depth, the total measured dose was found to agree with calculations within 2.1%. Overall, the dose delivered by each modalities, with the exception of the 6 MeV electrons, were within uncertainty of their respective calculated doses. The overall chamber dose measured on the Solid Water phantom was also found to agree within 0.73% ± 3.8% with calculations.

Figure 9 b) shows the SPR between the phantom material and air as a function of depth along the line shown in Fig. 9 a). The effect of the different material compositions on the SPR is clearly visible.

IV. DISCUSSION

The purpose of the film delivery on slabs of Solid Water phantom was to identify large errors in the planning, simulation and delivery process. The setup was inherently robust to positioning errors as the entire plan was delivered at a normal incidence to the flat phantom, therefore good agreement was expected between the film measurement and the simulated dose.

The cylindrical phantom delivery was set up to closely resemble the types of dose distributions obtainable for MBRT applications to soft tissue sarcomas of the leg. Electron dose distributions are known to be considerably more perturbed than photon dose distributions when delivered at oblique incidences; therefore, this delivery can be seen as a particularly challenging case for the electron MC beam models.

In both phantoms, the film measurements showed good overall agreement with gamma pass rates of 92% for a 2%/2 mm criteria. Although the 6 MeV component had poor agreement, this discrepancy can be attributed to the difficulty of precisely assigning an accurate film depth. At 2 cm depth, the film lies in the high gradient section of the depth dose curve of 6 MeV electrons. Small variations in depth ($\sim$1 mm) can thus cause large absolute dose shifts in the slice dose.

The difference between the total measured and simulated MBRT dose was -0.03% and 2.1% at a depth of 1.4 cm and 2.1 cm respectively. This discrepancy lies well within an expanded uncertainty ($k = 2$). As expected, the difference between measured and simulated absorbed doses was largest for the lowest energy electrons with discrepancies up to 26% at 6 MeV and depth of 2.1 cm. In addition to the accuracy of the MC models, the accuracy of the setup was expected to have a considerable impact on the delivered dose distribution. Although a mini ionisation chamber (A1SL, 0.053 cc) was used to perform all measurements, there remained large dose gradients inside the chamber volume, contributing to measurement uncertainty as the effective point of measurement is not well defined.

For MBRT plans, the dose distribution of each modality is often highly non-uniform within the PTV. This is because different modalities are usually covering different spatial regions of the PTV. For example, low energy electron components are usually responsible for the dose in superficial regions while photon doses are usually concentrated at edges of the PTV. As such, when performing ionisation chamber measurements, it is difficult to find a single point where the dose gradient is low for all modalities. In this study, although the point of measurement at 1.4 cm depth in the PMMA cylinder was located in a relatively high dose and low gradient region for the 12 MeV component, it was the opposite for the 6 MeV component. This larger dose gradient translates into a larger uncertainty on the measured dose of the 6 MeV component, as can be seen in Table V. Furthermore, the fidelity of the MC models is considerably worse at depths beyond the electron practical range (local discrepancies over 10% for doses below 1% of the maximum dose). As the 6 MeV apertures in the PMMA cylinder plan were predominantly delivered at gantry angles of $\pm 30^\circ$ (see Fig. 1), the effective depth of the point of measurement was larger than 3 cm, i.e. beyond the practical range. Comparing MC calculated doses at such depths to measurements would introduce systematic errors due to the inaccuracy of the MC model.

By calculating k_{MBRT} as a simple ratio of stopping power-ratios between measurement and reference conditions, we have implicitly assumed that P_{gr} was constant, which may explain part of the differences between measured and calculated doses. In addition, effects of electron fluence perturbation are ignored in our approach, which would affect the results predominantly at low electron energies (6 MeV and 9 MeV). The overall agreement between planned and delivered dose, however, confirms that for this situation the effects are limited.

The k_{MBRT} correction factor resulted in a 4% correction in measured dose for the highest electron energies. Despite k_{MBRT} being necessary for accurate measurements in MBRT conditions, we conclude that the measurement procedure followed in this work consists of a viable procedure for MBRT plan verification using an ionisation chamber.

Both MBRT plans were deliverable with a single setup procedure as the TrueBeam developer mode allows dynamic couch positioning. Changing between modalities was the longest overhead associated with MBRT compared to conventional photon radiation therapy. In both cases, the electron component of the plan was deliverable in less than 5 minutes, including modality changes, but not including setup time. In terms of beam-on time, all electron components can be delivered at a rate of 1000 MU/min, which speeds up delivery over the 600 MU/min maximum of photon beams with a flattening filter on the TrueBeam accelerator. The complete measurement process was performed in under 30 minutes. Using the methodology described in this paper, a more clinically practical patient-specific QA protocol will be developed based on point dose measurements.

As can be seen from table II, the number of monitor units per component greatly increases for the lower electron energies due to the fact that output factors degrade quickly for the combination of low energies and small fields. For example, we measured the 3×3 cm^2 MLC-defined field output factor to be 0.251 for 6 MeV, compared to 0.855 for 20 MeV. While the deliveries of these components is still accomplished rapidly due to the high dose rates achievable for electrons, Connell et al. found that electron output factors of FLEC-defined fields were highly sensitive to minute (≈ 0.5 mm) changes in jaws position when the field sizes were on the order of 3×3 cm^2 [8]. With pMLC-defined fields, this could also lead to large discrepancies between simulated and delivered doses if the linac jaws were miscalibrated. We therefore recommend that the MC-simulated output factors be compared to measured output factors regularly if MBRT plans are delivered with a substantial low energy electron component. By default, some manufacturers allow tolerances on MLC leaf positioning during treatment which could allow the beam to be enabled if the leaf is within, e.g., 2 mm of its intended position. For low electron beam energies and smaller MLC apertures, such tolerances could also lead to large differences in output factors. If possible, lower tolerances on MLC leaf positions should be used during MBRT delivery. Our preliminary investigation indicated that lower electron energies to be more sensitive to

small deviations in leaf positioning. In our Monte Carlo simulations, for nominal 3x3 cm^2 fields, the output factor of 6 MeV electrons increased by more than 6% when the field size was enlarged by 2 mm. For the same change in field size, higher electron energies had consistently lower output factor variation, such as less than 1% at 20 MeV.

The virtual SAD delivery of the electron components required a different couch position for each beam angle, which is not currently part of routine clinical practice. In an effort to produce plans which required fewer changes to current practice, we attempted to deliver the MBRT plans with a single couch position, hence a varying shortened SSD. However, with such a setup, the target volume is typically not on the beam central axis, leading to off-axis irradiation. The transition between beam angles therefore required large movements of the collimators, during which the beam had to be in the *beam hold* state. Beam holds on Varian accelerators are created by adjusting the grid voltage in the electron gun; during the beam hold state the accelerator is active with RF in the wave guide but the electron source is in a hold state. However, during the course of delivering these plans, we have discovered the presence of a persistent, low level of leakage radiation during the beam hold states which is high enough to trigger a machine interlock and interrupt the delivery.

A discussion with a representative from Varian Medical Systems confirmed that the leakage is due to the absence of attenuating material in the path of the beam compared to photon beams. This means that low electron currents in the waveguide can deliver appreciable doses to the patient even with the beam in the beam hold state. Virtual SAD deliveries result in less collimator movement which reduces the need for beam holds. However, long beam holds could still occur in virtual SAD deliveries if large collimator movements were needed, for example, if multiple physically separated small lesions were treated within the same session. A bigger engineering limitations of mixed beam deliveries is the time delay required when changing beam energy or particle. As a mixed beam plan can involve five electron energies and a photon component, adding a delay for each modality can considerably increase treatment times.

Although MBRT plans in this study were not robustly optimised, Renaud et al. (2019) [26] have shown that robust MBRT plans are necessary for deliveries of mixed electron-photon modalities in realistic clinical conditions. This however raises the question of how to perform QA on the robustness of a plan. Indeed, MBRT plans created using robust optimisation will no longer be robust to positioning errors when transposed onto measurement phantoms. Therefore, a study is necessary to determine the variation in agreement between simulated and measured doses from clinical robust plans delivered on QA phantoms and define realistic tolerances for QA setups of robust plans for the clinical site of interest.

V. CONCLUSION

The aim of this work was to confirm that the treatment plans produced by our MBRT treatment planning algorithm [16, 26] could be delivered and measured accurately on a Varian TrueBeam accelerator. In addition, we sought to develop the framework required for a potential patient-specific QA protocol.

These goals were first achieved by delivering a simple plan on slabs of Solid Water with a film placed at a depth of 2 cm, and comparing the results to the simulated delivery. The resulting gamma pass rate of 96.1% for a 3%/2 mm criteria confirmed that the MC beam models used in this work performed accurately.

A complex MBRT plan was delivered on a PMMA cylinder specifically constructed for ionisation chamber measurements and performing point dose measurements. A film measurement was also taken on an identically shaped phantom. The chamber measurement from each modality was corrected by a beam quality correction factor calculated using a MC code specifically created to obtain both dose distributions and correction factors with the same input in order to facilitate the QA process. The complete measurement procedure was realised in under 30 minutes, and the agreement between measured and simulated total dose agreed to within 2.1%, leading us to conclude that the procedure can be applied for clinical patient-specific QA.

VI. ACKNOWLEDGEMENTS

The authors would like to acknowledge Dr. Tanner Connell for helpful discussions on film measurements, Dr. James Renaud for assistance with reference dosimetry, and Joe Larkin for machining the phantom used in this work. The authors acknowledge support from the Fonds de recherche du Québec Nature et Technologie (FRQNT), the CREATE Medical Physics Research Training Network grant (number 432290) of the Natural Sciences and Engineering Research Council (NSERC) and the Canadian Institute of Health Research Foundation Grant (FDN-143257).

VII. CONFLICT OF INTEREST STATEMENT

The authors have no relevant conflicts of interest to disclose.

[1] M. C. Lee, S. B. Jiang, and C. M. Ma, "Monte Carlo and experimental investigations of multileaf collimated electron beams for modulated electron radiation therapy," *Medical Physics*, vol. 27, no. 12, pp. 2708–2718, 2000.

[2] C. M. Ma, T. Pawlicki, M. C. Lee, S. B. Jiang, J. S. Li, J. Deng, B. Yi, E. Mok, and A. L. Boyer, "Energy- and intensity-modulated electron beams for radiotherapy," *Physics in Medicine and Biology*, vol. 45, no. 8, pp. 2293–2311, 2000.

[3] K. R. Hogstrom, R. A. Boyd, J. A. Antolak, M. M. Svatos, B. A. Faddegon, and J. G. Rosenman, "Dosimetry of a prototype retractable eMLC for fixed-beam electron therapy," *Medical Physics*, vol. 31, no. 3, pp. 443–462, 2004.

[4] T. Gauer, D. Albers, F. Cremers, R. Harmansa, R. Pellegrini, and R. Schmidt, "Design of a computer-controlled multileaf collimator for advanced electron radiotherapy," *Physics in Medicine and Biology*, vol. 51, no. 23, pp. 5987–6003, 2006.

[5] T. Gauer, J. Sokoll, F. Cremers, R. Harmansa, M. Luzzara, and R. Schmidt, "Characterization of an add-on multileaf collimator for electron beam therapy," *Physics in Medicine and Biology*, vol. 53, no. 4, pp. 1071–1085, 2008.

[6] K. Al-Yahya, F. Verhaegen, and J. Seuntjens, "Design and dosimetry of a few leaf electron collimator for energy modulated electron therapy," *Medical Physics*, vol. 34, no. 12, pp. 4782–4791, 2007.

[7] A. Alexander, F. Deblois, and J. Seuntjens, "Toward automatic field selection and planning using Monte Carlo-based direct aperture optimization in modulated electron radiotherapy," *Physics in Medicine and Biology*, vol. 55, no. 16, pp. 4563–4576, 2010.

[8] T. Connell, A. Alexander, P. Papaconstadopoulos, M. Serban, S. Devic, and J. Seuntjens, "Delivery validation of an automated modulated electron radiotherapy plan," *Medical Physics*, vol. 41, no. 6, 2014.

[9] F. C. Du Plessis, A. Leal, S. Stathakis, W. Xiong, and C. M. Ma, "Characterization of megavoltage electron beams delivered through a photon multi-leaf collimator (pMLC)," *Physics in Medicine and Biology*, vol. 51, no. 8, pp. 2113–2129, 2006.

[10] E. E. Klein, M. Vicic, C. M. Ma, D. A. Low, and R. E. Drzymala, "Validation of calculations for electrons modulated with conventional photon multileaf collimators," *Physics in Medicine and Biology*, vol. 53, no. 5, pp. 1183–1208, 2008.

[11] F. J. Salguero, B. Palma, R. Arrans, J. Rosello, and A. Leal, "Modulated electron radiotherapy treatment planning using a photon multileaf collimator for post-mastectomized chest walls," *Radiotherapy and Oncology*, vol. 93, no. 3, pp. 625–632, 2009.

[12] D. Henzen, P. Manser, D. Frei, W. Volken, H. Neuenschwander, E. J. Born, a. Joosten, K. Lössl, D. M. Aebersold, C. Chatelain, M. F. M. Stampanoni, and M. K. Fix, "Beamlet based direct aperture optimization for MERT using a photon MLC.," *Medical physics*, vol. 41, p. 121711, dec 2014.

[13] E. E. Klein, Z. Li, and D. A. Low, "Feasibility study of multileaf collimated electrons with a scattering foil based accelerator," *Radiotherapy and Oncology*, vol. 41, no. 2, pp. 189–196, 1996.

[14] A. Alexander, E. Soisson, M.-A. Renaud, and J. Seuntjens, "Direct aperture optimization for FLEC-based MERT and its application in mixed beam radiotherapy.," *Medical physics*, vol. 39, pp. 4820–31, aug 2012.

[15] B. A. Palma, A. U. Sánchez, F. J. Salguero, R. Arráns, C. M. Sánchez, A. W. Zurita, M. I. R. Hermida, and A. Leal, "Combined modulated electron and photon beams planned by a Monte-Carlo-based optimization procedure for accelerated partial breast irradiation," *Physics in Medicine and Biology*, vol. 57, no. 5, pp. 1191–1202, 2012.

[16] M.-A. Renaud, M. Serban, and J. Seuntjens, "On mixed electron-photon radiation therapy optimization using the column generation approach," *Medical Physics*, vol. 44, no. 8, pp. 4287–4298, 2017.

[17] S. Mueller, M. K. Fix, A. Joosten, D. Henzen, D. Frei, W. Volken, R. Kueng, D. M. Aebersold, M. F. Stampanoni, and P. Manser, "Simultaneous optimization of photons and electrons for mixed beam radiotherapy," *Physics in Medicine and Biology*, vol. 62, no. 14, pp. 5840–5860, 2017.

[18] S. Mueller, P. Manser, W. Volken, D. Frei, R. Kueng, E. Herrmann, O. Elicin, D. M. Aebersold, M. F. M. Stampanoni, and M. K. Fix, "Part 2: Dynamic mixed beam radiotherapy (dymber): Photon dynamic trajectories combined with modulated electron beams," *Medical Physics*, vol. 45, no. 9, pp. 4213–4226, 2018.

[19] C. Míguez, E. Jiménez-Ortega, B. A. Palma, H. Miras, A. Ureba, R. Arráns, F. Carrasco-Peña, A. Illescas-Vacas, and A. Leal, "Clinical implementation of combined modulated electron and photon beams with conventional MLC for accelerated partial breast irradiation," *Radiotherapy and Oncology*, vol. 124, no. 1, pp. 124–129, 2017.

[20] P. R. Almond, P. J. Biggs, B. M. Coursey, W. F. Hanson, M. S. Huq, R. Nath, and D. W. Rogers, "AAPM's TG-51 protocol for clinical reference dosimetry of high-energy photon and electron beams," *Medical Physics*, vol. 26, no. 9, pp. 1847–1870, 1999.

[21] B. R. Muir and D. W. Rogers, "Monte Carlo calculations of electron beam quality conversion factors for several ion chamber types," *Medical Physics*, vol. 41, no. 11, p. 111701, 2014.

[22] B. R. Muir and D. W. Rogers, "Monte Carlo calculations of kQ, the beam quality conversion factor," *Medical Physics*, vol. 37, no. 11, pp. 5939–5950, 2010.

[23] M. McEwen, L. Dewerd, G. Ibbott, D. Followill, D. W. Rogers, S. Seltzer, and J. Seuntjens, "Addendum to the AAPM's TG-51 protocol for clinical reference dosimetry of high-energy photon beams," *Medical Physics*, vol. 41, no. 4, 2014.

[24] P. Andreo, D. T. Burns, A. E. Nahum, J. Seuntjens, and F. H. Attix, *Fundamentals of ionizing radiation dosimetry*. John Wiley & Sons, 2017.
[25] D. W. O. Rogers, I. Kawrakow, J. P. Seuntjens, B. R. B. Walters, and E. Mainegra-Hing, "NRC User Codes for EGSnrc," tech. rep., National Research Council of Canada, 2003.
[26] M.-A. Renaud, M. Serban, and J. Seuntjens, "Robust mixed electron-photon radiation therapy optimisation," *Medical Physics*, vol. 0, no. ja, 2019.
[27] A. Rodrigues, D. Sawkey, F. F. Yin, and Q. Wu, "A Monte Carlo simulation framework for electron beam dose calculations using Varian phase space files for TrueBeam Linacs," *Medical Physics*, vol. 42, no. 5, pp. 2389–2403, 2015.
[28] D. W. O. Rogers, B. Walters, and I. Kawrakow, "BEAMnrc Users Manual," tech. rep., National Research Council of Canada, 2011.
[29] B. Walters, I. Kawrakow, and D. W. O. Rogers, "DOSXYZnrc Users Manual," tech. rep., National Research Council of Canada, 2016.
[30] J. Lobo and I. A. Popescu, "Two new DOSXYZnrc sources for 4D Monte Carlo simulations of continuously variable beam configurations, with applications to RapidArc, VMAT, TomoTherapy and CyberKnife," *Physics in Medicine and Biology*, vol. 55, no. 16, pp. 4431–4443, 2010.
[31] C. M. Ma, R. A. Price, J. S. Li, L. Chen, L. Wang, E. Fourkal, L. Qin, and J. Yang, "Monitor unit calculation for Monte Carlo treatment planning," *Physics in Medicine and Biology*, vol. 49, no. 9, pp. 1671–1687, 2004.
[32] S. A. Lloyd, I. M. Gagne, M. Bazalova-Carter, and S. Zavgorodni, "Measured and Monte Carlo simulated electron backscatter to the monitor chamber for the Varian TrueBeam Linac," *Physics in Medicine and Biology*, vol. 61, no. 24, pp. 8779–8793, 2016.
[33] P. Sipilä, J. Ojala, S. Kaijaluoto, I. Jokelainen, and A. Kosunen, "Gafchromic ebt3 film dosimetry in electron beams — energy dependence and improved film read-out," *Journal of Applied Clinical Medical Physics*, vol. 17, no. 1, pp. 360–373, 2016.
[34] INTERNATIONAL ATOMIC ENERGY AGENCY, *Absorbed Dose Determination in External Beam Radiotherapy*. No. 398 in Technical Reports Series, Vienna: INTERNATIONAL ATOMIC ENERGY AGENCY, 2000.
[35] M. Miften, A. Olch, D. Mihailidis, J. Moran, T. Pawlicki, A. Molineu, H. Li, K. Wijesooriya, J. Shi, P. Xia, N. Papanikolaou, and D. A. Low, "Tolerance limits and methodologies for imrt measurement-based verification qa: Recommendations of aapm task group no. 218," *Medical Physics*, vol. 45, no. 4, pp. e53–e83, 2018.

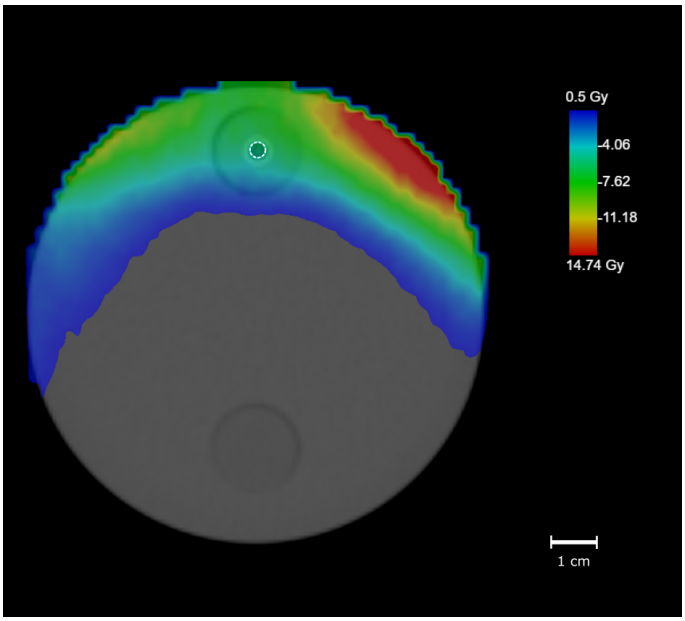

FIG. 1. Dose colourwash for the 6 MeV component of a MBRT plan delivered on a PMMA phantom. The beam quality of particles inside the chamber air cavity (shown as in dotted white lines) will differ substantially from the beam quality at reference conditions.

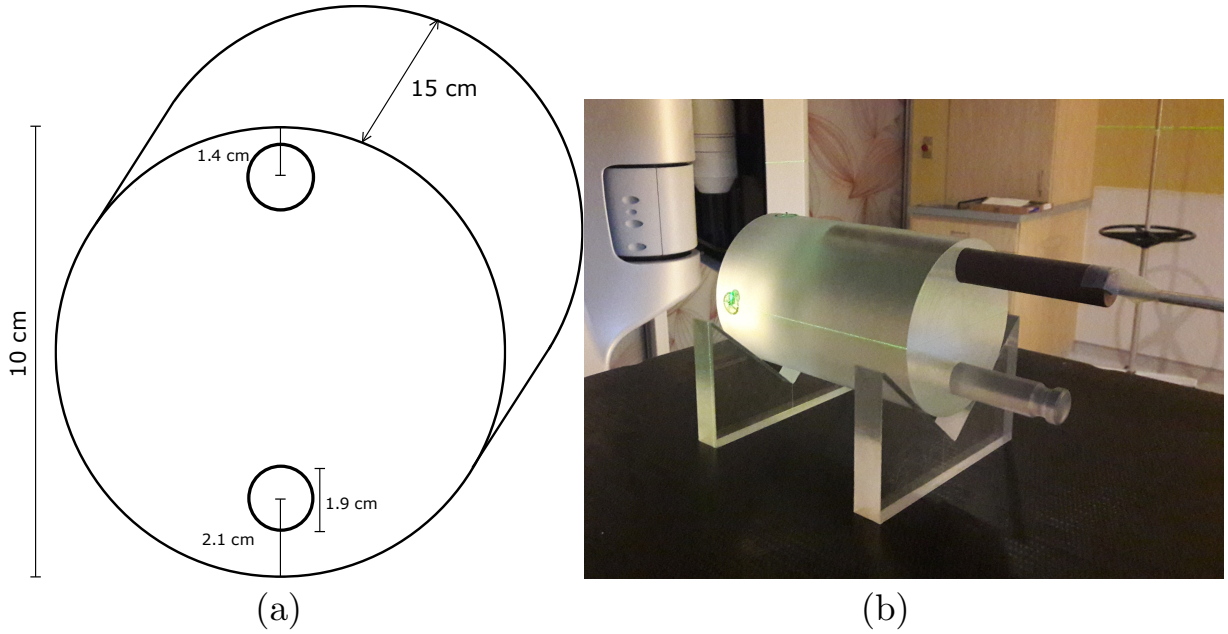

FIG. 2. (a) Schematic diagram of the PMMA cylinder machined for ionisation chamber measurements. (b) Setup of the PMMA cylinder for chamber measurement.

TABLE I. Summary of the planned beam delivery angles and phantom positions. Gantry angles are given in the range of -180° to 180°, with 0° corresponding to the gantry being in its exactly vertical position. A rotation from $-110° \rightarrow 110°$ corresponds to $250° \rightarrow 110°$ in the Varian IEC 601-2-1 convention. * The shortened electron SAD is realised in practice as a virtual SAD, meaning that the couch is moved such that the centre of the target is 80 cm from the source for each beam angle.

	Solid water plan	PMMA cylinder plan
Photon angles (°)	arc from −110 to 110	arc from −110 to 110
Electron angles (°)	0	$(-30, 0, 30)$
Photon SAD (cm)	100	100
Electron SAD (cm)*	80	80

TABLE III. Beam quality specifiers and conversion factors for each electron beam energy for the Exradin A1SL ion chamber [21], measured in a water tank using a 10x10 cm^2 MLC-defined field at 80 cm SSD. $k_{Q,ecal}$ for the A1SL was taken to be 0.914. The SPRs were calculated using SPRXYZnrc with a Type A uncertainty of less than 0.2%. An uncertainty of 1.1% on the reference absorbed dose per monitor unit was assessed using the same uncertainty budget approach as detailed in McEwen et al. [23].

Energy (MeV)	R_{50} (cm)	d_{ref} (cm)	k'_Q	$(SPR^w_{air})_Q$	D_{ref} (cGy / MU)
6	2.46	1.38	1.0318	1.079	1.498 ± 0.016
9	3.70	2.12	1.0197	1.062	1.508 ± 0.016
12	5.10	2.96	1.0104	1.045	1.518 ± 0.016
16	6.73	3.94	1.0024	1.034	1.487 ± 0.016
20	8.31	4.89	0.9963	1.023	1.426 ± 0.015

TABLE II. Distribution of monitor units per modality for the two plans delivered in this work, normalised to deliver 50 Gy to 95% of the contoured target volume.

	Monitor units per modality					
Plan	6 MeV	9 MeV	12 MeV	16 MeV	20 MeV	6 MV
Solid Water	4410	12035	5290	0	0	9264
PMMA	8118	1033	1707	1126	1898	2598

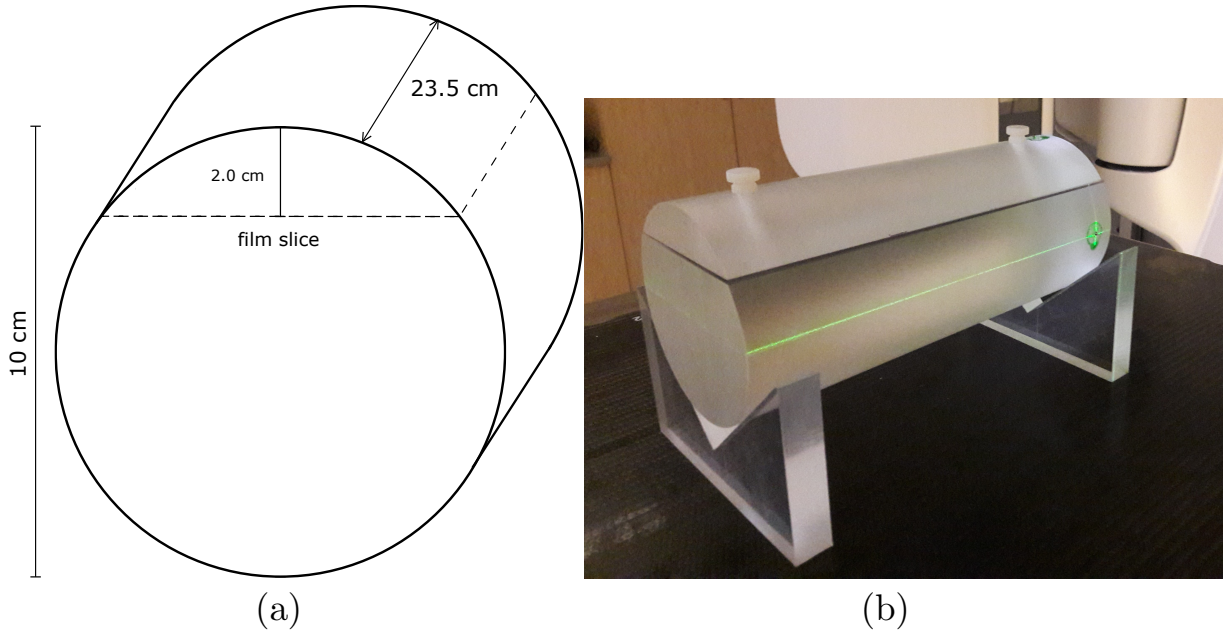

FIG. 3. (a) Schematic diagram of the PMMA cylinder machined for film measurements. (b) Setup of the PMMA cylinder sliced for film measurement at 2 cm depth.

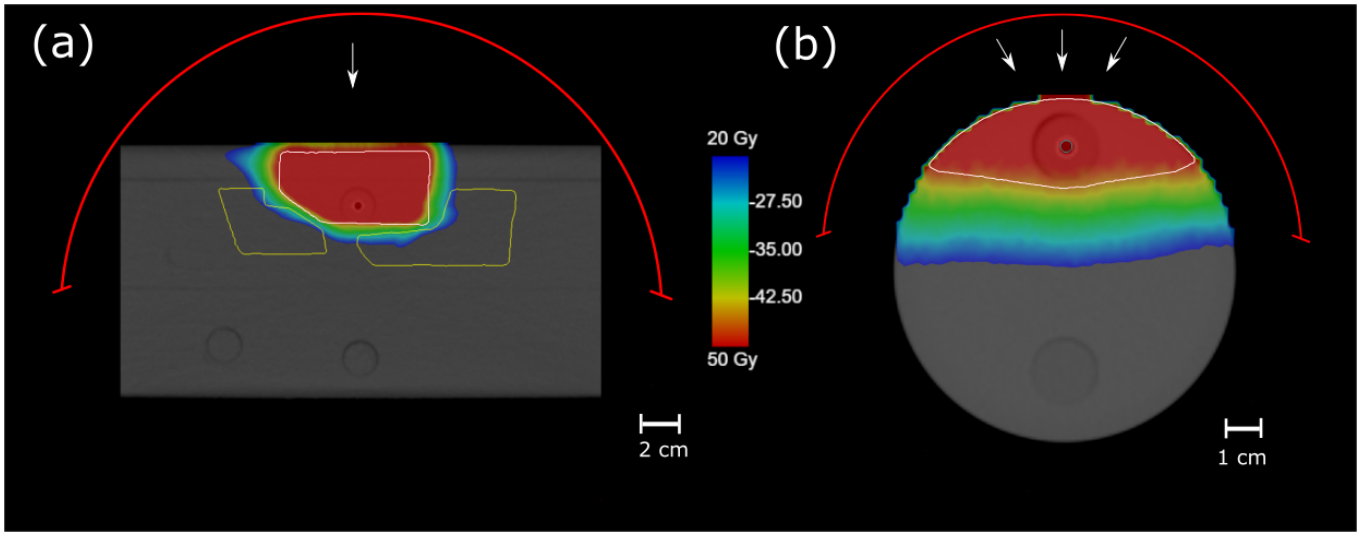

FIG. 4. Dose colourwash for a representative axial slice of the (a) simplified MBRT plan delivered on Solid Water slabs and (b) complex MBRT plan delivered on the PMMA cylinder. In both cases, the target is shown as a white contour. The yellow contours in (a) represents hypothetical OARs. The red arcs correspond to the range of gantry angle at which photon beams are delivered. Similarly, white arrows are the gantry angles of electron beams.

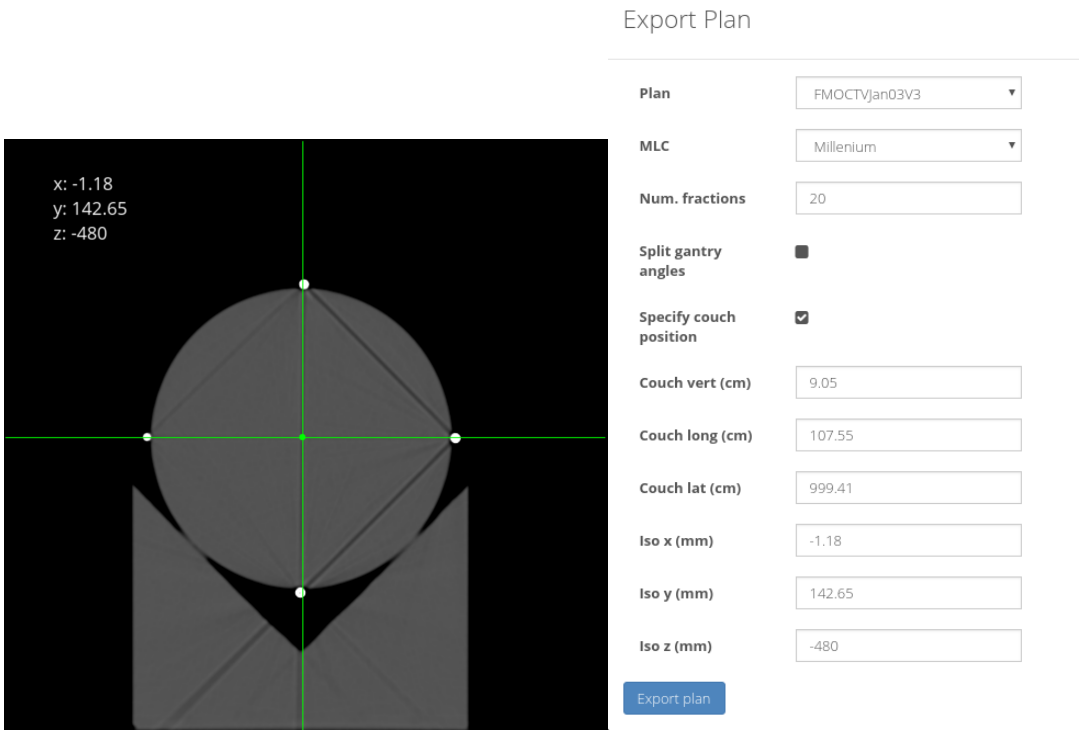

FIG. 5. (a) Identification of the machine isocenter position in the CT coordinate system when the phantom BBs are aligned with the in-room lasers. (b) Example of the information supplied by the user when exporting a plan as developer mode XML files from our in-house TPS.

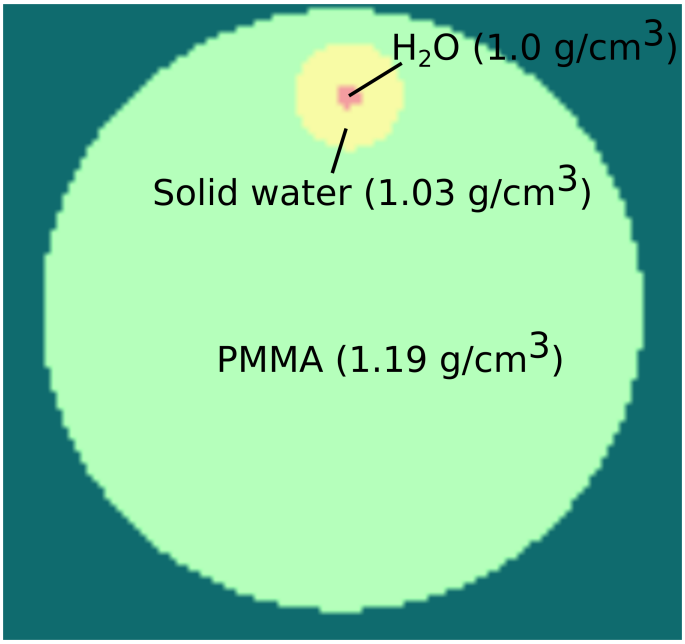

FIG. 6. MC phantom materials and densities used to calculate the dose inside the ionisation chamber placed at 1.4 cm depth.

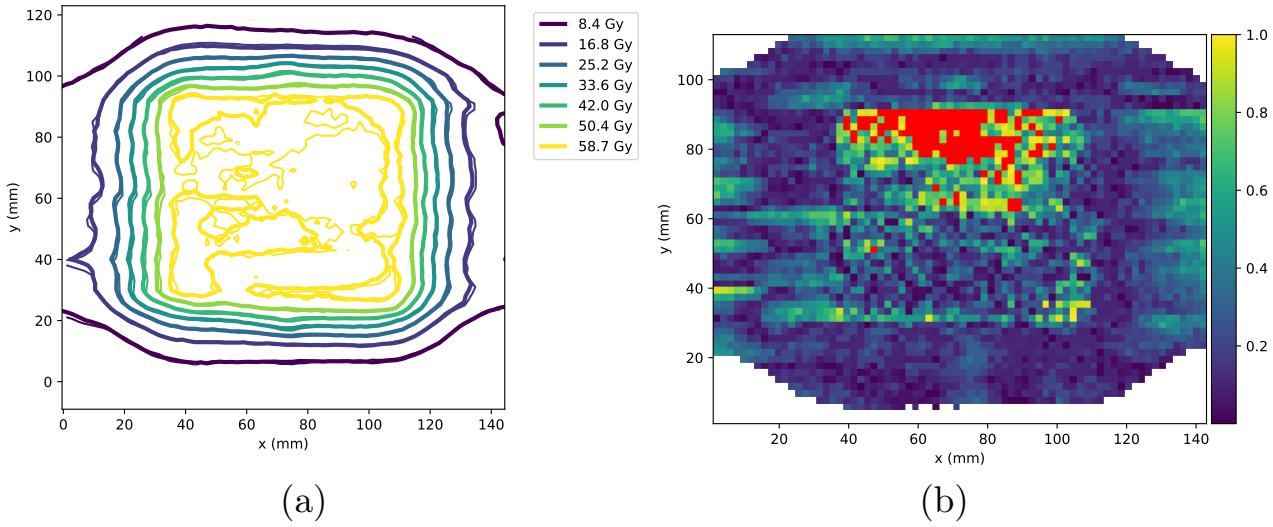

FIG. 7. (a) Isodose comparison between measured film dose (thin lines) and simulated dose (thick lines) for the overall delivery on the Solid Water slabs. (b) Gamma map for a 3% / 2 mm passing criteria. Pixels in red have $\gamma \geq 1$.

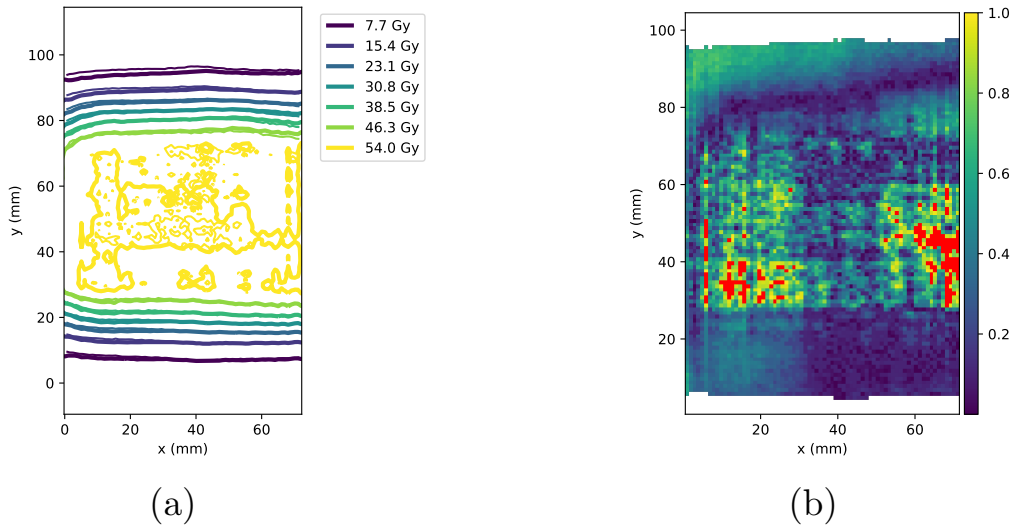

FIG. 8. (a) Isodose comparison between measured film dose (thin lines) and simulated dose (thick lines) for the overall delivery on the cylindrical PMMA phantom. (b) Gamma map for a 3% / 2 mm passing criteria. Pixels in red have $\gamma \geq 1$.

TABLE IV. Film global gamma passing rates for delivery on cylindrical PMMA and flat Solid Water phantom.

	Pass rate criterion	20 MeV	16 MeV	12 MeV	9 MeV	6 MeV	6 MV	Overall
PMMA phantom	3%/2mm (%)	98	99.8	98.8	98.7	84.6	99.2	97.3
	2%/2mm (%)	95.8	98.4	96.4	96.9	62.1	96.8	92.5
		Overall (6 MV, 6 MeV, 9 MeV, 12 MeV)						
Solid Water phantom	3%/2mm (%)	96.1						
	2%/2mm (%)	92.2						

TABLE V. Measurement data from an Exradin A1SL ionisation chamber placed in the 1.4 cm insert of the PMMA phantom compared to simulated MC doses. The measurement doses were corrected for the beam quality at the measurement point using k_{MBRT}. The uncertainty on k_{MBRT} is estimated at 1%, dominated by the type B uncertainty associated with neglecting the cavity fluence perturbation. Uncertainties are presented with a coverage factor $k = 1$.

Depth: 1.4 cm	20 MeV	16 MeV	12 MeV	9 MeV	6 MeV	6 MV	Electrons	Total
$\left(\frac{\bar{L}}{\rho}\right)^{w}_{air}$	0.984	0.996	1.015	1.043	1.088	1.120		
k_{MBRT}	0.962	0.966	0.971	0.982	1.008	0.999		
D_{meas} (Gy)	9.59 ± 0.33	9.48 ± 0.39	14.14 ± 0.29	7.81 ± 0.4	5.88 ± 0.47	6.20 ± 0.12	46.90 ± 0.85	53.09 ± 0.86
D_{MC} (Gy)	9.53 ± 0.14	9.52 ± 0.14	14.31 ± 0.21	7.93 ± 0.12	5.39 ± 0.08	6.43 ± 0.06	46.68 ± 0.33	53.11 ± 0.33
ΔD (%)	-0.5 ± 3.8	-0.4 ± 4.4	-1.2 ± 2.6	-1.5 ± 5.4	8.3 ± 7.5	-3.8 ± 2.2	0.5 ± 1.9	-0.0 ± 1.7
Depth: 2.1 cm	20 MeV	16 MeV	12 MeV	9 MeV	6 MeV	6 MV	Electrons	Total
$\left(\frac{\bar{L}}{\rho}\right)^{w}_{air}$	0.991	1.008	1.03	1.066	1.11	1.119		
k_{MBRT}	0.969	0.978	0.986	1.004	1.029	0.998		
D_{meas} (Gy)	9.93 ± 0.37	9.09 ± 0.29	14.74 ± 0.34	7.73 ± 0.31	3.53 ± 0.75	6.68 ± 0.31	45.01 ± 0.75	51.69 ± 0.76
D_{MC} (Gy)	10.03 ± 0.15	8.86 ± 0.13	14.43 ± 0.22	8.06 ± 0.12	2.54 ± 0.04	6.72 ± 0.07	43.91 ± 0.32	50.63 ± 0.33
ΔD (%)	-1.0 ± 4.1	2.6 ± 3.5	2.1 ± 2.7	-4.2 ± 4.4	28 ± 15	-0.6 ± 4.8	2.4 ± 1.8	2.1 ± 1.6

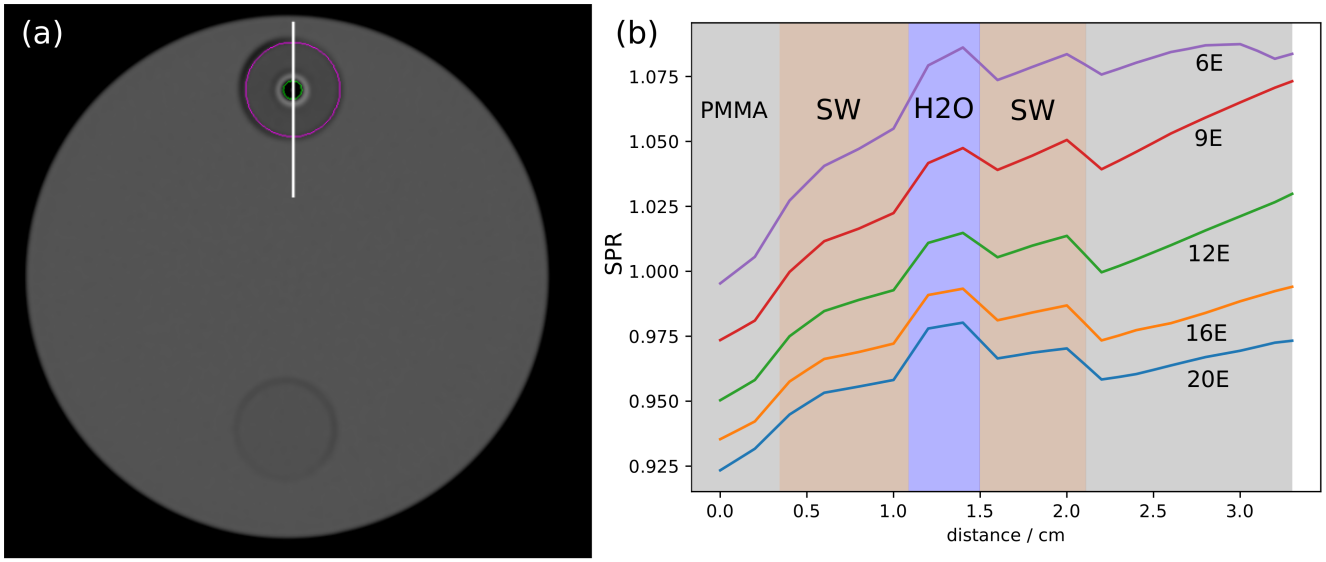

FIG. 9. (a) Axial CT slice of the PMMA phantom showing the line along which the SPRs are plotted for each modality. (b) SPR between the phantom medium and air. The active volume of the ionisation chamber was modelled as water.